




Thermal-field electron emission from three-dimensional Dirac and Weyl semimetalsWei Jie Chan , Yee Sin Ang *, and L. K. Ang †*Science, Mathematics and Technology (SMT), Singapore University of Technology and Design (SUTD), 8 Somapah Road, 487372 Singapore*

(Received 17 May 2021; accepted 23 November 2021; published 20 December 2021)

A model is constructed to describe the thermal-field emission of electrons from a three-dimensional (3D) Dirac and Weyl semimetal hosting Dirac/Weyl node(s). The traditional thermal-field electron emission model is generalized to accommodate the 3D nonparabolic energy band structures in the Dirac/Weyl semimetals, such as cadmium arsenide (Cd_3As_2), sodium bismuthide (Na_3Bi), tantalum arsenide (TaAs), and tantalum phosphide (TaP). Due to the nontrivial energy decomposition of the energy dispersion and the vanishing transverse density of states, an unusual dual-peak feature is observed in the total energy distribution spectrum. This nontrivial dual-peak feature, absent from traditional materials, plays a critical role in manipulating the magnitude of the emission current through the variation of an applied field, temperature, and Fermi level. This feature suggests that a higher Fermi level will achieve a larger current density (apart from low work function). At zero temperature limit, a F^3 scaling law for pure field emission is derived and it is different from the well-known Fowler-Nordheim F^2 scaling law. Furthermore, these new behaviors have shown to exist beyond the Dirac cone approximated model. This model expands the recent understandings of electron emission studied for the Dirac two-dimensional (2D) materials into the 3D regime, and thus offers a theoretical foundation for the exploration in using Dirac semimetallic materials as novel electrodes.

DOI: [10.1103/PhysRevB.104.245420](https://doi.org/10.1103/PhysRevB.104.245420)**I. INTRODUCTION**

Dirac/Weyl semimetals (D/WSM)s, a subset of Dirac materials, have been studied rapidly over the past decade [1–10] due to its electronic [11–14], optical [14–17], and magnetic [14,17,18] properties. The unconventional band structures about its Dirac point have brought about many interesting applications in electronics [19–21], spintronics [22], photonics [23,24], nonlinear optics [25–27], and topological electronics (topotronics) [28]. Apart from these applications, the physics of electron emission from Dirac materials like carbon-based nanomaterials [29–31] or graphene [32–41] have also received attention over the past two decades.

Field-induced electron emission describes the quantum tunneling of electrons from a material surface into a vacuum under a strong electric field. The most well-known field emission physics is described by the Fowler-Nordheim (FN) based models developed for traditional bulk materials [42–44]. Compared to the conventional field emitters [45–50], these novel quantum materials exhibit Dirac conic band structure about its Fermi level with nonparabolic energy dispersion [9], and have also been experimentally shown to exhibit large field enhancement and stable current emission [51–53]. However, the physics of thermal-field emission of some recently discovered quantum materials (such as 3D Dirac/Weyl semimetals) has not been studied in detail, which immediately leads to the following questions: (i) How can the conventional thermal-field emission model be generalized to accommodate

the nonparabolic band structure of Dirac and Weyl semimetals? (ii) How does the Dirac conic band structure affect the thermal-field emission behaviors of 3D D/WSM? (iii) What key differences can be observed for a D/WSM emitter in terms of their current, voltage, and temperature scaling laws at both the field and thermal-field emission regimes?

In this paper, we address the above questions by constructing a generalized thermal-field emission model for the newly discovered 3D D/WSMs. In particular, the total energy distribution (TED) and the emission current density are calculated. Our model applies the Dirac cone approximation for D/WSMs and considers the Schottky-Nordheim (SN) barrier [42,54] at the material-vacuum interface, as seen in Fig. 1(a). The electron emission can reside from either the conduction (orange) or valence (blue) bands and are then replenished (purple) at the intrinsic Fermi level ε_{F0} . The differing (linear) energy dispersion from a Dirac cone allows us to study the thermal-field emission of 3D DSMs/WSMs. Due to the nontrivial decomposition of the energy dispersion and the vanishing transverse density of states (TDOS), we predict an unconventional feature in the TED, and a new F^3 scaling law at the zero temperature limit, which is different from the FN law. Consequently, the presence of this nontrivial feature produces an additional requirement, a higher Fermi level, for a larger emission current (apart from having a low work function). Furthermore, by tuning the applied electric field strength, temperature, and Fermi level of a D/WSM emitter, we can manipulate the magnitude of the emission current density through the energy profile of the TED. These findings can pave the way for the theoretical study of other Dirac materials, in particular, materials that are described by Dirac cone(s) and Weyl nodes in the band structure, which

*yeesin_ang@sutd.edu.sg

†ricky_ang@sutd.edu.sg

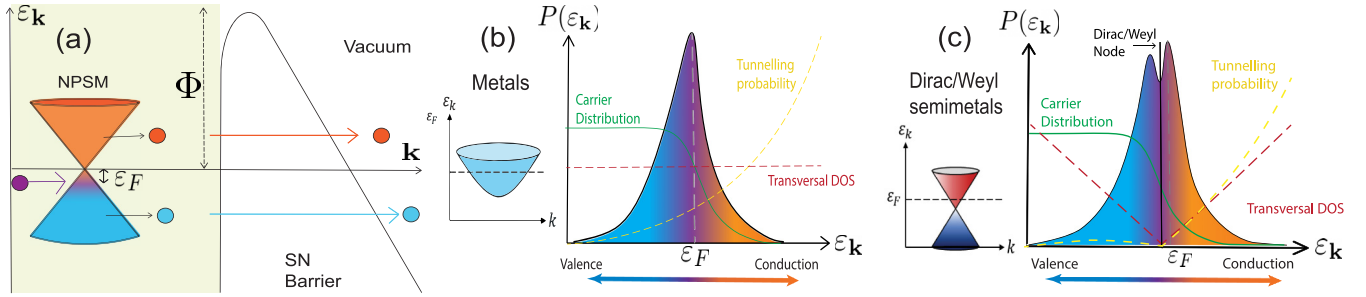


FIG. 1. (a) Schematic diagram of a material with a linear dispersion under the Dirac cone approximation. Under an electric field, the electrons emit through a Schottky-Nordheim (SN) barrier [54] with work function Φ into vacuum. Orange/blue electrons are emitted, respectively, from the conduction/valence bands. The emitted electrons are then replenished at the Fermi level ε_F (gray dotted line) immediately by replacement electrons (purple) entering the Dirac cone [47]. The relationship of the energy dispersion, carrier density (green solid line), tunneling probability (yellow dotted line), and in particular, the transverse density of states (DOS) (red dotted line), help sculpt the total energy distribution (TED) $P(\varepsilon_{\mathbf{k}})$ of (b) a conventional metal with a parabolic dispersion, giving us a single peak TED, and (c) of a DSM/WSM using the Dirac cone approximation, giving us a dual-peak feature in the TED. The vertical black solid line in (c) represents the location of the Dirac or Weyl node in the $\varepsilon_{\mathbf{k}}$ space.

cannot be modeled by the traditional thermal-field emission models [54].

II. GENERALIZED THERMAL-FIELD EMISSION MODEL

A. Generalized emission current density

We consider a generalized thermal-field electron emission model in the form of

$$\mathcal{J}_{\perp} = \frac{eg}{(2\pi)^3} \int v_{\perp}(\varepsilon_{\mathbf{k}}) f(\varepsilon_{\mathbf{k}}) \mathcal{T}(\varepsilon_{\perp}) d^3\mathbf{k}, \quad (1)$$

where \mathcal{J}_{\perp} is the electron current density emitted vertically from a surface, e is the charge of an electron, g is the degeneracy factor, $f(\varepsilon_{\mathbf{k}})$ is the Fermi-Dirac distribution function, and $\mathcal{T}(\varepsilon_{\perp})$ is the tunneling probability. The group velocity along the emitting direction (denoted as \perp) is

$$v_{\perp}(\varepsilon_{\mathbf{k}}) = \frac{1}{\hbar} \frac{\partial \varepsilon_{\mathbf{k}}}{\partial k_{\perp}}. \quad (2)$$

In the following, we define \perp to be pointing in the z direction and \parallel along the x - y plane. The tunneling probability \mathcal{T} in Eq. (1) can be modeled after the SN barrier model [42,54] to account for the image charge potential, given by

$$\mathcal{T}(\varepsilon_{\perp}) \approx D_F \exp\left\{\frac{\varepsilon_{\perp} - \varepsilon_F}{d_F}\right\}, \quad (3)$$

where $D_F \equiv \exp(-bv\sqrt{\Phi^3}/F)$ is the tunneling exponent term and $d_F \equiv 2F/3b\sqrt{\Phi\tau}$ is the decay width of the wave function through the barrier, $b = 4\sqrt{2m}/3e\hbar$ is a Fowler-Nordheim (FN) constant [43] with m being the electron mass, Φ is the work function of the material, and F is the applied field. The image charge effect can be approximated with the following correction terms [42]:

$$v \approx 1 - f_s + \frac{f_s}{6} \ln f_s, \quad \tau \approx 1 + \frac{f_s}{9} - \frac{f_s}{18} \ln f_s, \quad (4)$$

with $f_s = e^3 F / 4\pi \epsilon_0 \Phi^2$, where ϵ_0 is the vacuum permittivity.

B. Generalized thermal-field models for nonparabolic energy dispersion

To accommodate the nonparabolic energy dispersion, we transform Eq. (1) into an alternative form. We first consider a generic energy dispersion $\varepsilon_{\mathbf{k}}[\varepsilon_{\parallel}(\mathbf{k}_{\parallel}), \varepsilon_{\perp}(\mathbf{k}_{\perp})]$ with $\varepsilon_{\parallel}(\mathbf{k}_{\parallel})$ and $\varepsilon_{\perp}(\mathbf{k}_{\perp})$ as the energy component transverse and along the tunneling direction, respectively. By rewriting Eq. (1) in terms of the \perp and the \parallel components through $d^3\mathbf{k} = k_{\parallel} dk_{\parallel} d\phi_{\mathbf{k}_{\parallel}} dk_{\perp}$, with $\phi_{\mathbf{k}_{\parallel}} = \tan^{-1}(k_y/k_x)$, we have

$$\mathcal{J}_{\perp} = \frac{ge}{(2\pi)^3 \hbar} \iiint f(\varepsilon_{\mathbf{k}}) \mathcal{T}(\varepsilon_{\perp}) \frac{\Lambda_{\perp}}{\Lambda_{\parallel}} d\varepsilon_{\perp} d\phi_{\mathbf{k}_{\parallel}} d\varepsilon_{\parallel}, \quad (5)$$

where the following transformation identity is used:

$$\frac{\partial \varepsilon_{\mathbf{k}}}{\partial |k_{\perp}|} \mathbf{k}_{\parallel} dk_{\parallel} dk_{\perp} = \frac{\partial \varepsilon_{\mathbf{k}}}{\partial \varepsilon_{\perp}} d\varepsilon_{\perp} \frac{k_{\parallel}}{\partial \varepsilon_{\parallel} / \partial k_{\parallel}} d\varepsilon_{\parallel}.$$

This allow the definition of the energy dispersion factors as

$$(\Lambda_{\perp}, \Lambda_{\parallel}) \equiv \left(\frac{\partial \varepsilon_{\mathbf{k}}}{\partial \varepsilon_{\perp}}, \frac{1}{k_{\parallel}} \frac{d\varepsilon_{\parallel}}{dk_{\parallel}} \right), \quad (6)$$

where Λ_{\perp} is only nontrivial with the existence of a nonparabolic dispersion, while Λ_{\parallel} encapsulates the transverse density of states (TDOS). These energy dispersion factors in Eq. (6) play crucial roles in understanding the electron field emission with nonparabolic energy dispersion.

Consider an isotropic 3D parabolic energy dispersion $\varepsilon_{\mathbf{k}} = \hbar^2(k_{\parallel}^2 + k_{\perp}^2)/2m$ where m is the electron effective mass and $\mathbf{k} = (\mathbf{k}_{\parallel}, \mathbf{k}_{\perp})$ with \mathbf{k}_{\parallel} representing the wave vector component transverse to the emission direction, the total energy is *partitioned* into the emission component $\varepsilon_{\perp} \equiv \hbar^2 k_{\perp}^2 / 2m$, the transverse component $\varepsilon_{\parallel} \equiv \hbar^2 k_{\parallel}^2 / 2m$, and $\varepsilon_{\mathbf{k}} = \varepsilon_{\parallel} + \varepsilon_{\perp}$. In doing so, Eq. (6) becomes

$$(\Lambda_{\perp}, \Lambda_{\parallel})^{\text{parabolic}} \equiv \left(1, \frac{\hbar^2}{m} \right), \quad (7)$$

which is a constant term (independent of ε_{\parallel} and ε_{\perp}). Solving Eq. (1) with Eq. (7) will yield the classic Fowler-Nordheim (FN) law for cold field emission, and the Murphy-Good (MG) model for thermal-field emission.

For a nonparabolic (or linear) energy dispersion, we have

$$\varepsilon_{\mathbf{k}} = \sqrt{\varepsilon_{\mathbf{k}\perp}^2 + \varepsilon_{\mathbf{k}\parallel}^2}. \quad (8)$$

For Dirac/Weyl semimetals (D/WSMs), the quasiparticles around the Dirac point(s) are described by the effective Hamiltonian $\mathcal{H}_{\mathbf{k}} = \hbar \sum_{i,a} v_{Fi,a} k_{i,a} \sigma_i$ where $i = \{x, y, z\}$ and σ_i is the Pauli matrix along \hat{i} and the subscript a labels the a th Dirac cone [9,57,58,60,61]. The energy dispersion of these Dirac/Weyl semimetals (SM) is

$$\varepsilon_{\mathbf{k}}^{\text{SM}} = \sum_{a=1}^N \sqrt{\sum_i \hbar^2 v_{Fi,a}^2 k_{i,a}^2}, \quad (9)$$

where $\varepsilon_{\parallel,a} \equiv \hbar(v_{Fx,a}^2 k_{x,a}^2 + v_{Fy,a}^2 k_{y,a}^2)^{1/2}$ and $\varepsilon_{\perp,a} \equiv \hbar v_{Fz,a} |k_{z,a}|$. The corresponding energy dispersion factors for a Dirac conic dispersion are

$$(\Lambda_{\perp,a}, \Lambda_{\parallel,a})^{\text{SM}} \equiv \left(\frac{\varepsilon_{\perp,a}}{\varepsilon_{\mathbf{k},a}}, \frac{\hbar^2 \tilde{v}_a^2}{\varepsilon_{\parallel,a}} \right), \quad (10)$$

where $\tilde{v}_a \equiv v_{Fy,a} \sqrt{(v_{Fx,a}/v_{Fy,a})^2 \cos^2 \phi_{\mathbf{k}\parallel,a} + \sin^2 \phi_{\mathbf{k}\parallel,a}}$, a is the Fermi velocity along the \parallel direction. This is in stark contrast to the parabolic dispersion case as shown in Eq. (7) and will lead to a drastically different thermal-field emission characteristics for D/WSMs to be reported below.

III. THERMAL-FIELD EMISSION FROM DIRAC AND WEYL SEMIMETALS

A. Emission current density and scaling law from Dirac cones

For an isotropic parabolic energy dispersion, Eq. (5) can be simplified as

$$\mathcal{J}_{\perp}^{\text{parabolic}} = \frac{g_s m e}{(2\pi)^2 \hbar^3} \int f(\varepsilon_{\mathbf{k}}) \mathcal{T}(\varepsilon_{\perp}) d\varepsilon_{\perp} d\varepsilon_{\mathbf{k}}, \quad (11)$$

g_s is the spin degeneracy, $\frac{\partial \varepsilon_{\mathbf{k}}}{\partial \varepsilon_{\mu}} = 1$, $\mu \in \{\perp, \parallel\}$ which can be approximately solved to yield the well-known Murphy-Good (MG) thermal-field emission model [54]:

$$\mathcal{J}_{\perp}^{\text{MG}} = \frac{a_{\text{FN}} F^2}{\Phi t^2} D_F \frac{k_B T \pi / d_F}{\sin(k_B T \pi / d_F)}, \quad (12)$$

where $a_{\text{FN}} = e^3 / (16\pi^2 \hbar)$ is the FN constant and k_B is the Boltzmann constant.

The FN plot (for FN scaling) can be obtained by rearranging Eq. (12) such that

$$\ln \left(\frac{\mathcal{J}_{\perp}^{\text{MG}}}{F^2} \right) = -\frac{bv\sqrt{\Phi^3}}{F} + \ln \left(\frac{a_{\text{FN}} k_B T \pi / d_F}{\Phi t^2 \sin(k_B T \pi / d_F)} \right). \quad (13)$$

At $T = 0$ K (cold field emission), it recovers the classical FN scaling of $\ln(\mathcal{J}_{\perp}^{\text{MG}}/F^2) \propto -1/F$. Note the F^2 component in the logarithm term is a signature of field emission from 3D bulk materials.

In contrast, Eq. (5) of a D/WSM exhibits a nontrivial difference due to Eq. (10). This difference is first seen from

Eq. (2) which can be written as

$$\mathcal{J}_{\perp}^{\text{SM}} = \sum_{a=1}^N \frac{g_a e}{(2\pi \hbar)^3} \int \left(\int |\varepsilon_{\perp,a}| \mathcal{T}(\varepsilon_{\perp,a}) f(\varepsilon_{\mathbf{k},a}) d\varepsilon_{\perp,a} \right) d\varepsilon_{\mathbf{k},a} \times \left(\int \frac{d\phi_{\mathbf{k}\parallel,a}}{\tilde{v}_a^2} \right), \quad (14)$$

where $\partial \varepsilon_{\mathbf{k}} / \partial \varepsilon_{\parallel} = \varepsilon_{\parallel} / \varepsilon_{\mathbf{k}}$ is used and $\varepsilon_{\perp} \rightarrow |\varepsilon_{\perp}|$ can be made as the emission energy is non-negative. g_a is the spin and node degeneracy for each contributing Dirac cone, N is the number of contributing Dirac cone(s) to the emission. The $d\phi_{\mathbf{k}\parallel,a}$ integration is simply 2π for an isotropic dispersion and $2\pi / (v_x v_y)$ for an anisotropic dispersion as derived in Appendix A. Equation (14) can be further simplified and numerically solved as

$$\mathcal{J}_{\perp}^{\text{SM}} = \sum_{a=1}^N \frac{c_{\text{SM},a} F^2}{\Phi t^2} D_F \int_{-\infty}^{\infty} f(\varepsilon_{\mathbf{k},a}) \lambda(\varepsilon_{\mathbf{k},a}/d_F) d\varepsilon_{\mathbf{k},a}, \quad (15)$$

where $c_{\text{SM},a} = e^3 g_a / (32m\pi^2 \hbar v_{Fx,a} v_{Fy,a})$ is a constant. The dimensionless tunneling function $\lambda(\varepsilon_{\mathbf{k},a}/d_F)$ is defined as

$$\lambda(\varepsilon_{\mathbf{k},a}/d_F) = \exp \left\{ \frac{\varepsilon_{\mathbf{k},a} - \varepsilon_F}{d_F} \right\} \left(\frac{\varepsilon_{\mathbf{k},a}}{d_F} - 1 \right) \text{sgn}(\varepsilon_{\mathbf{k},a}) + \frac{1 + \text{sgn}(\varepsilon_{\mathbf{k},a})}{2}. \quad (16)$$

The FN plot now takes the form of

$$\ln \left(\frac{\mathcal{J}_{\perp}^{\text{SM}}}{F^2} \right) = -\frac{bv\sqrt{\Phi^3}}{F} + \sum_{a=1}^N \left[\ln \left(\frac{c_{\text{SM},a}}{\Phi t^2} \right) + \ln \left(\int_{-\infty}^{\infty} f(\varepsilon_{\mathbf{k},a}) \lambda(\varepsilon_{\mathbf{k},a}/d_F) d\varepsilon_{\mathbf{k},a} \right) \right]. \quad (17)$$

At $T = 0$ K (cold field emission), Eq. (15) becomes

$$\mathcal{J}_{\perp,T=0}^{\text{SM}} = \sum_{a=1}^N \frac{c_{\text{SM},a} D_F}{\sqrt{\Phi^3} t^2} F^3 \left(\frac{\varepsilon_F}{d_F} - 1 \right), \quad (18)$$

where $c_{\text{SM},a} = 4c_{\text{SM},a}/3$. The scaling law at $T = 0$ then becomes

$$\ln \left(\frac{\mathcal{J}_{\perp,T=0}^{\text{SM}}}{F^3} \right) = -\frac{bv\sqrt{\Phi^3}}{F} + \sum_{a=1}^N \ln \left[\frac{c_{\text{SM},a}}{\sqrt{\Phi^3} t^2} \left(\frac{\varepsilon_F}{d_F} - 1 \right) \right], \quad (19)$$

Thus, this produces an unexpected scaling of

$$\ln \left(\frac{\mathcal{J}_{\perp}^{\text{SM}}}{F^3} \right) \propto -\frac{1}{F}, \quad (20)$$

which is different from the classical FN scaling of $\ln(\mathcal{J}_{\perp}^{\text{MG}}/F^2) \propto -1/F$ for bulk solids with parabolic dispersion.

B. Total energy distribution (TED) of Dirac cones

The energy spectrum of the emitted electrons is determined from the total energy distribution (TED): $P(\varepsilon_{\mathbf{k}})$ by considering $\partial \mathcal{J}_{\perp} / \partial \varepsilon_{\mathbf{k}}$ such that

$$P(\varepsilon_{\mathbf{k}}) d\varepsilon_{\mathbf{k}} = \frac{g e}{(2\pi \hbar)^3} \left(\int f(\varepsilon_{\mathbf{k}}) \mathcal{T}(\varepsilon_{\perp}) \frac{\Lambda_{\perp}}{\Lambda_{\parallel}} d\varepsilon_{\perp} d\phi_{\mathbf{k}\parallel} \right) d\varepsilon_{\mathbf{k}}, \quad (21)$$

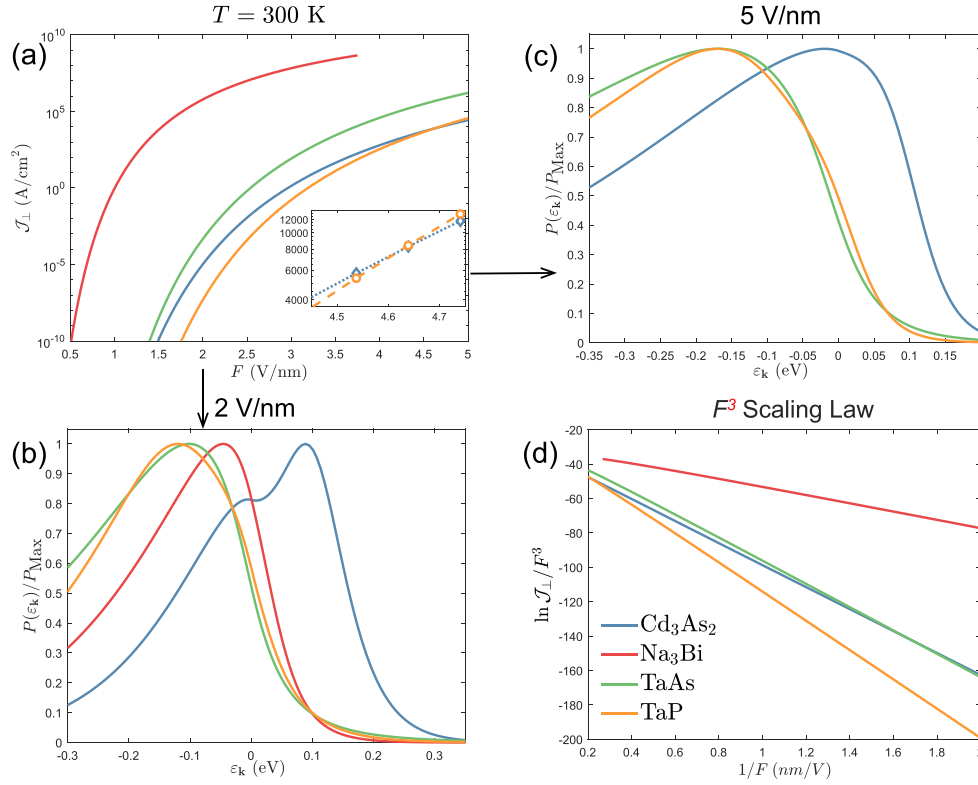


FIG. 2. The emission current density \mathcal{J}_\perp is plotted at room temperature (300 K) in (a) for Cd_3As_2 (blue), Na_3Bi (red), TaAs (green), and TaP (orange). The inset is a magnified plot showing the overtaking of \mathcal{J}_\perp for Cd_3As_2 over TaP at high fields. The \mathcal{J}_\perp line for Na_3Bi terminates after 3.84 V/nm to indicate the transition from field emission to field-induced ballistic emission [62]. By fixing $F = 2$ V/nm in (b), and $F = 5$ V/nm in (c), the normalized total energy distributions (TEDs) (with respect to its peak) $P(\epsilon_{\mathbf{k}})/P_{\text{Max}}$ of these four semimetals are plotted. The dual-peak feature is only visible for Cd_3As_2 in (b). The F^3 scaling law is plotted in (d) for all aforementioned D/WSMs. Due to the termination in (a), the Na_3Bi plot does not appear in (c) and does not start from 0.2 (V/nm) $^{-1}$ in (d).

where the transverse density of states is $D(\epsilon_{\mathbf{k}}) = g/[(2\pi)^2\Lambda_\parallel(\epsilon_{\mathbf{k}})]$ with $\int D(\epsilon_\parallel)d\phi_{\mathbf{k}_\parallel}d\epsilon_\parallel = \int D(\epsilon_{\mathbf{k}})d\phi_{\mathbf{k}_\parallel}d\epsilon_{\mathbf{k}}$.

With a constant transverse density of states (TDOS) and a trivial decomposition of the dispersion, the TED of 3D bulk metallic material takes on a conventional single peak behavior as seen in Fig. 1(b). This is due to the trivial energy dispersion factors $\Lambda_\perp/\Lambda_\parallel$ in Eq. (7), which gives a constant TDOS, i.e., $D(\epsilon_{\mathbf{k}}) = gm/(2\pi\hbar)^2$, and an exponential tunneling probability to achieve the well-known MG TED,

$$P^{\text{MG}}(\epsilon_{\mathbf{k}}) = c_T \frac{F}{\sqrt{\Phi t}} D_F f(\epsilon_{\mathbf{k}}) \exp\left\{\frac{\epsilon_{\mathbf{k}} - \epsilon_F}{d_F}\right\}. \quad (22)$$

On the contrary, Eq. (10) produces a nontrivial ϵ_\perp and ϵ_\parallel dependence term in its energy dispersion factors as illustrated in Fig. 1(c). The additional ϵ_\perp dependence in Λ_\perp in Eq. (14) have a vanishing tunneling probability (yellow dotted line) at the vicinity of the Dirac/Weyl node (black solid line), which produces a nontrivial tunneling function in Eq. (16). Likewise, the additional $\epsilon_\parallel \rightarrow \epsilon_{\mathbf{k}}$ dependence in Λ_\parallel produces a vanishing TDOS (red dotted line), i.e., $D(\epsilon_{\mathbf{k}}) = g\epsilon_{\mathbf{k},a}/(2\pi\hbar\tilde{v}_a)^2$. Notably, these two factors must appear simultaneously to prevent the occurrence of a singularity (unphysical) in the TED from $\Lambda_\perp/\Lambda_\parallel$ in Eq. (21). The product of these two factors with the Fermi-Dirac distribution (green solid line) can produce a distinctive dual-peak feature in the vicinity of the

Dirac or Weyl node in the TED of a D/WSM, i.e.,

$$P^{\text{SM}}(\epsilon_{\mathbf{k}}) = \sum_{a=1}^N \frac{c_{\text{SM},a} F^2}{\Phi t^2} D_F f(\epsilon_{\mathbf{k},a}) \lambda(\epsilon_{\mathbf{k},a}/d_F). \quad (23)$$

This shows that the key ingredients to the dual-peak feature are the existence of a nontrivial decomposition of the energy dispersion and the vanishing TDOS. As seen below, this unconventional behavior in Eq. (23) is only present under a range of parameters, and have implications towards the emission current density.

Notably, the dual-peak feature and the F^3 scaling law from Eq. (20) are not artifacts from the Dirac cone approximation. This is shown in Appendix B, where a physical TED proportional to Eq. (23) can be derived due to the nontrivial decomposition of the dispersion and the vanishing TDOS for a realistic Hamiltonian for both Dirac and Weyl semimetals [63–65].

IV. RESULTS

A. Additional criteria for larger current density and unconventional scaling law

In Fig. 2(a) the emission current densities \mathcal{J}_\perp in Eq. (15) are plotted against F for two DSMs, Cd_3As_2 (blue) and Na_3Bi (red), and two WSMs, TaAs (orange) and TaP (green),

TABLE I. Material parameters of the DSM: Cd₃As₂ and Na₃Bi, and WSMs: TaAs and TaP, are listed in this table. The parameters consists of the work function Φ , the energy difference of the intrinsic Fermi level ε_{F0} from the Dirac or Weyl node(s) at $\varepsilon_{\mathbf{k}} = 0$, the Fermi velocities in the transverse direction v_{Fx} and v_{Fy} , and the degeneracies of the nodes in the dispersion space g . WSMs must have at least a pair of distinct Weyl nodes [9].

DSMs/WSMs	Φ (eV)	ε_{F0} (eV)	v_{Fx} (10 ⁶ m/s)	v_{Fy} (10 ⁶ m/s)	g
Cd ₃ As ₂ ^a	4.5	0.1	1.3	1.28	4
Na ₃ Bi ^b	2.35	0.025	0.374	0.374	4
TaAs ^c	4.65	-0.0221, -0.0089	0.250,0.240	0.120,0.350	8,16
TaP ^d	5.405	-0.0531, 0.0196	0.310,0.230	0.150,0.300	8,16

^aReferences [6,8,55,56].

^bReferences [7,55].

^cReferences [57–59].

^dReferences [57,59].

with the materials parameters shown in Table I. Notably, the abnormally large magnitude of \mathcal{J} is due to the low work function Φ of Na₃Bi. These emitters can transit to the ballistic field emission regime at lower F values. However, ballistic emission cannot be accurately modeled within the framework of the MG model [62]. Hence, the upper bound of \mathcal{J}_{\perp} for Na₃Bi is approximately given by $F = 0.695\Phi^2/(\text{eV})^2 \approx 3.84$ V/nm [62].

Apart from the expected proportional increase of \mathcal{J}_{\perp} with F , the Φ dependency, i.e., $\mathcal{J}_{\perp} \propto -1/\Phi$, does not follow except for $F > 4.6$ V/nm as highlighted in the inset for both Cd₃As₂ and TaP. This is attributed to the relationship between vanishing TDOS in the Dirac conic dispersion and the intrinsic Fermi level ε_{F0} of a D/WSM. Indeed, as the height of the potential barrier is gradually lowered, the dependency of $D_F\lambda(\varepsilon_{\mathbf{k}}/d_F)$ in Eq. (23) makes it easier for carriers below the ε_{F0} to tunnel across the surface barrier. However, this also gradually allows the carriers in the vicinity of the vanishing TDOS, below the ε_{F0} for Cd₃As₂, to dominate the emission process, which suppresses the increment of the current density.

Particularly, only Cd₃As₂ have the dual-peak feature in the normalized (with respect to their peaks) TEDs for $F < 4.6$ V/nm as shown in Fig. 2(b) for 2 V/nm. This can be resolved by further lowering the barrier height, which allow the carriers in the lower Dirac cone to dominate the emission process. As evident in Fig. 2(c) at $F = 5$ V/nm, the normalized TEDs do not have the aforementioned feature, which explains why D/WSMs satisfy the $\mathcal{J}_{\perp} \propto 1/\Phi$ relation for higher F . Comparatively, D/WSMs with lower ε_{F0} can activate the lower Dirac cone with a lower F , which is evident by the lack of the nontrivial feature even at 2 V/nm. Hence, an additional criterion (higher ε_{F0}) apart from a lower Φ is required for emitting a larger \mathcal{J}_{\perp} from a D/WSM emitter. Notably, Na₃Bi is not plotted here as $F > 3.84$ V/nm.

Interestingly, Fig. 2(d) shows that the field emission follows an unconventional scaling of $\ln(\mathcal{J}_{\perp}/F^3) \propto -1/F$ [Eq. (20)] for all D/WSMs. The excellent linearity of $\ln(\mathcal{J}_{\perp}/F^3) \propto -1/F$ reveals that a D/WSM emitter follows an unconventional non-FN scaling not commonly seen in traditional materials, i.e., $\ln(\mathcal{J}_{\perp}/F^2)$. Similarly, the gradual crossover of the Cd₃As₂ scaling with TaAs and TaP is due to the aforementioned criteria. Notably, Na₃Bi does not start from $1/F = 0.2$ (V/nm)⁻¹ due to the transition.

B. Functional control of emission current density

Next, as the thermal-field \mathcal{J}_{\perp} does not scale much with T , the $\mathcal{J}_{\perp}/\mathcal{J}_0$ is plotted instead in Fig. 3(a) at 2 V/nm. \mathcal{J}_0 is defined to be the zero-temperature \mathcal{J}_{\perp} and is chosen as the normalization term to highlight the nontrivial behavior under low T , which is enlarged in the inset. \mathcal{J}_{\perp} increases proportionally with T as expected from Eq. (15) for Cd₃As₂ and TaP at 2 V/nm. For an emitter with a higher ε_{F0} like Cd₃As₂, the suppression from the dual-peak feature is present and away from the peak of the TED, which implies that the increment of T will not be detrimental to its \mathcal{J}_{\perp} .

Interestingly, this differs for TaP as both of its Weyl nodes have ε_{F0} lower than Na₃Bi. However, unlike TaAs, TaP has a Weyl node above and below the Fermi level (Table I). This can be understood near half-filling (10 K), where the carriers from the Dirac cone with $\varepsilon_{F0} = 0.0196$ eV, reduce the suppression from the dual-peak feature from the Dirac cone with $\varepsilon_{F0} = -0.0531$ eV, and hence forming an obvious plateau in Fig. 3(b). This effect magnifies at higher T for TaP which is reinforced by the increment and the lack of suppression of \mathcal{J}_{\perp} in the inset of Fig. 3(a).

In contrast, the existence of a minimal $\mathcal{J}_{\perp} \neq \mathcal{J}_0$ for both Na₃Bi and TaAs implies that \mathcal{J}_{\perp} is heavily suppressed with increasing T , as highlighted in the inset of Fig. 3(a). This is reinforced by Fig. 3(b), where the dual-peak feature is close to the maxima of the TED, which signifies the suppression of the majority of its carriers.

Although the magnitude of \mathcal{J}_{\perp} can be recovered to at least \mathcal{J}_0 at $T(\mathcal{J}_0)$, it becomes increasingly harder with increasing F as seen in Fig. 3(c). Indeed, the lowering of the barrier height allows the suppressed region to have a higher emission probability, as regulated by $D_F\lambda(\varepsilon_{\mathbf{k}}/d_F)$ in Eq. (15). Hence, additional thermal energy is required to include more carriers from the upper Dirac cone to dampen the effect of the suppression of \mathcal{J}_{\perp} from the dual-peak feature in the TED. As shown in Fig. 3(d) for Na₃Bi and TaAs at 300 K (solid line) and 3.5 V/nm, the normalized TEDs have broad widths and do not have the dual-peak feature, unlike at 10 K (dotted line). Notably, the suppression is even greater for TaAs due to the existence of an additional Weyl node below ε_{F0} , as evident by the node summation in Eq. (15) and the small plateau in the normalized TED, which implies the suppression of carriers even below the Weyl nodes at very low T .

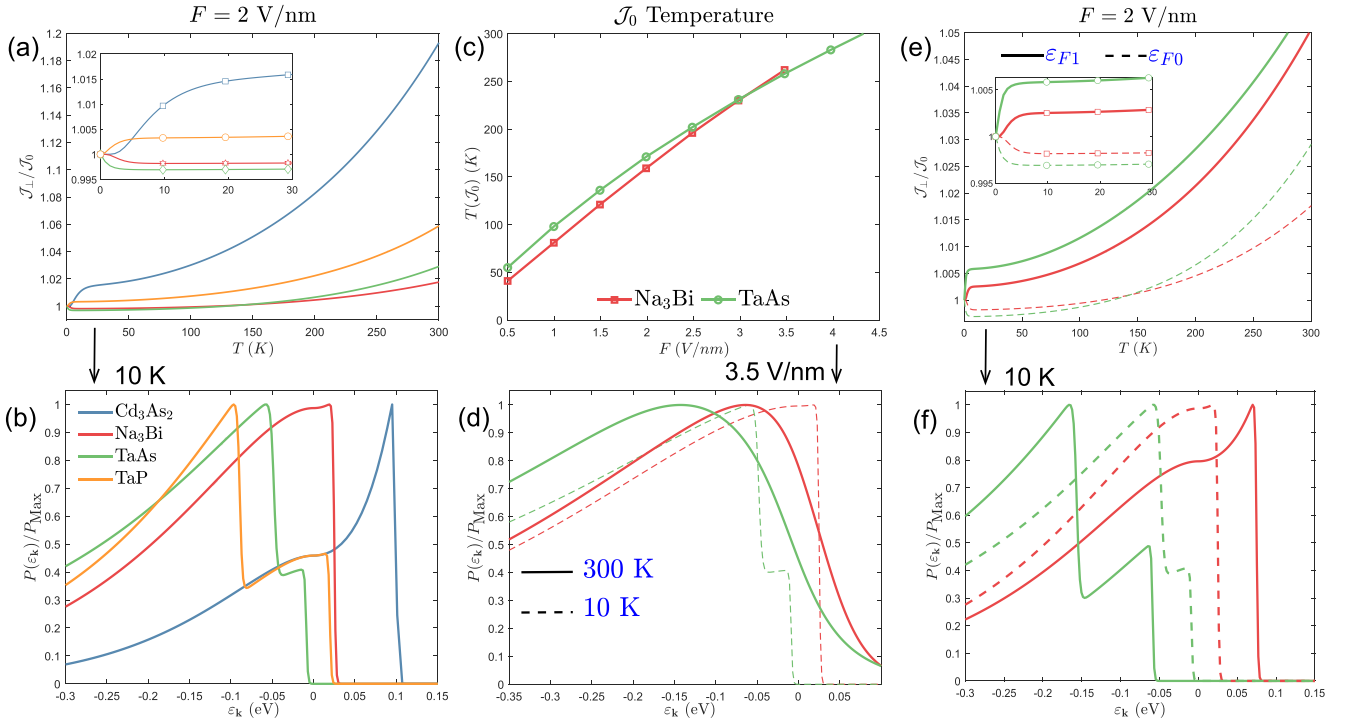


FIG. 3. The normalized emission current density $\mathcal{J}_\perp/\mathcal{J}_0$ are plotted for Cd_3As_2 (blue), Na_3Bi (red), TaAs (green), and TaP (orange) at 2 V/nm in (a) with \mathcal{J}_0 defined as the zero temperature emission current density. The inset highlights the low temperature behavior, particularly showing a decrease in \mathcal{J}_\perp for both Na_3Bi and TaAs . The markers in the inset are plotted for visual purposes. By fixing $T = 10$ K, the normalized total energy distribution (TED) (with respect to peak) $P(\mathbf{k})/P_{\text{Max}}$, are plotted in (b). Evidently the dual-peak feature for both Na_3Bi and TaAs are nearer to the peak as compared to both Cd_3As_2 and TaP . The temperature at which \mathcal{J}_0 can be recovered, i.e., $T(\mathcal{J}_0)$ for both Na_3Bi and TaAs while varying F is plotted in (c). By fixing $F = 3.5$ V/nm, the normalized TEDs of Na_3Bi and TaAs are plotted for 300 K (solid line) and 10 K (dotted line). Note that Na_3Bi terminates at $F = 3.84$ V/nm as it becomes ballistic at higher fields. Evidently the dual-peak feature is only visible at $T = 10$ K, below the $T(\mathcal{J}_0)$ lines in (d). The effects of the variation of $\epsilon_{F0} \rightarrow \epsilon_{F1}$ (dotted and solid lines, respectively) are plotted in (e) and (f) for Na_3Bi (+0.05 eV) and TaAs (-0.05 eV). In (e), the Fermi level shifting clearly removes the decrease of \mathcal{J}_\perp at low T as seen for $F = 2$ V/nm. This is supported by (f), where the dual-peak feature in the normalized TEDs shift away from the peak of the TEDs when the Fermi level is varied from ϵ_{F0} to ϵ_{F1} .

Apart from increasing T , the suppression of \mathcal{J}_\perp can be removed by varying (either increasing or decreasing) the Fermi level ϵ_F for Na_3Bi and TaAs . To illustrate this, $\mathcal{J}_\perp/\mathcal{J}_0$ is plotted for Na_3Bi at $\epsilon_{F0} + 0.05$ eV and TaAs at $\epsilon_{F0} - 0.05$ eV (both solid lines) and compared against its ϵ_{F0} counterparts (dotted line) in Fig. 3(e). Indeed, by shifting the Fermi level away from the nodes in either direction, the low T suppression is mitigated as shown in the inset. This is further reinforced by the contrasting normalized TEDs in Fig. 3(f), where the dual-peak feature is shifted away from the peak of the TED of Na_3Bi and is absent for TaAs due to the lack of thermal excited carriers. A drawback however for the lowering of ϵ_F is the reduction of \mathcal{J}_\perp . Thus, the variation of F , T , and ϵ_F can act as a functional control for \mathcal{J}_\perp through the dual-peak feature in the TED of the D/WSM emitter.

V. DISCUSSION

In this work, the thermal-field emission of D/WSM are modeled under a Dirac cone and the general behavior is also extended up to $O(k^2)$ in Appendix B. However, there are several other theoretical considerations and proposals that can be further discussed for experimental implementations.

First, the nontrivial feature in the TED in Eq. (23) and the F^3 scaling law in Eq. (17) can be extended to other gapless semimetals as long as it satisfies the two factors discussed in Sec. III B. An example can be gapless semimetallic bismuth, which exhibits a parabolic dispersion along z and a linear dispersion along both x and y [66]. Indeed, the vanishing TDOS and nontrivial decomposition of the energy dispersion comes from the gapless bulk state and the differing dispersion along different spatial axis, respectively.

Second, under the bulk emitter assumption, F is assumed to not penetrate the bulk states, which indicates that the energy scale for emitting Dirac electrons can be modeled up to 460 K for these materials. Beyond this energy scale, the thermal-field emission include massless Kane electrons for Cd_3As_2 and Na_3Bi [67], which can bring about nontrivial consequences to the field emission quantities.

Lastly, even though these four materials have been shown to exhibit protected topologically protected surface states, i.e., Fermi arcs [6,7,9,10,12,26,57,64], it has been predicted that these Fermi arcs will diffuse into the bulk states for a topological Dirac or Weyl semimetal under a strong electric field (orders of V/nm) [68]. These Fermi arcs can be preserved and contribute to field emission by lowering the field strength

to below 10 V/ μm . This implies that the Fermi arcs can only be determined within the transition region between the thermionic and field emission [54], which cannot be described by the current model. Alternatively, a topological DSM phase was experimentally achieved within 0.1 V/nm for Cd₃As₂ and Na₃Bi thin film emitters [69]. Hence, these Fermi arcs can be safely assumed to be diffused into the bulk states, and hence not contributing within the thermal-field emission regime for 3D bulk D/WSM emitters.

VI. CONCLUSION

In conclusion, a thermal-field emission model for 3D Dirac semimetal (DSM) and Weyl semimetal (WSM) with a linear Dirac conic energy dispersion have been developed in this work, with particular emphasis on Cd₃As₂, Na₃Bi, TaAs, and TaP. Our results predict the existence of a new $\ln(J/F^3) \propto -1/F$ scaling law and a nontrivial dual-peak feature in the total energy distribution (TED), which is absent in an electron field emitter composed of traditional metals with a conventional 3D parabolic energy band structure. The differing scaling law stresses the importance of this current work for D/WSM emitters as compared to the traditional Murphy and Good model [54]. The dual-peak feature stems from the nontrivial decomposition of the energy dispersion and the vanishing transverse density of states in the Dirac conic dispersion, which enforces an additional requirement (apart from a lower work function), a higher Fermi level, for a larger emission current density.

Furthermore, the functional control of the emission current density is intertwined with the dual-peak feature in the TED through the variation of the applied field, temperature, and Fermi level. This highlights the vital role of this feature in regulating the emission current density. The low work function of Na₃Bi can be beneficial for field emission application due to its high emission current density and its experimentally achievable field ballistic emission transition. With the additional criteria, Cd₃As₂ with its sufficiently high Fermi level (despite a higher work function), is also a suitable candidate for achieving a larger emission current density. Although that TaP can generate a higher emission current density than TaAs, the material consideration of a Weyl semimetallic emitter is highly dependent on each contributing Weyl node. Dirac semimetallic emitters with high work functions and low Fermi levels, however, can still achieve a relatively larger emission current density by exploiting the high sensitivity of the dual-peak feature with the variation of F , T , and ε_F . Finally, we remark that our model does not consider effects such as field-induced topological effects [9,14,68–70], band bending [71], space charge [72,73], and Fermi velocity shifting [59,68]. Such effects could be included in future works to investigate their roles on the thermal-field emission characteristics of 3D D/WSM.

ACKNOWLEDGMENTS

This work is funded by MOE Tier 2 (2018-T2-1-007) and A*STAR AME IRG (A2083c0057). Y.S.A. is supported by SUTD Startup Grant (SRG SCI 2021 163). W.J.C. acknowledges MOE Ph.D. RSS.

APPENDIX A: DERIVATION OF TOTAL ENERGY DISTRIBUTION (TED) AND EMISSION CURRENT DENSITY (\mathcal{J}_\perp) FOR DSM/WSM(S)

The generalized emission electrical current density from a 3D bulk electron emitter with a linear (nonparabolic) dispersion is shown in Eq. (5) of Sec. II as

$$\mathcal{J}_\perp^L = \frac{ge}{(2\pi)^3 \hbar} \iiint f(\varepsilon_{\mathbf{k}}) \mathcal{T}(\varepsilon_\perp) \frac{\Lambda_\perp}{\Lambda_\parallel} d\varepsilon_\perp d\phi_{\mathbf{k}_\parallel} d\varepsilon_\parallel, \quad (\text{A1})$$

where the superscript L indicates a linear dispersion. Inserting Eq. (10) into Eq. (5) gives Eq. (14),

$$\mathcal{J}_\perp^{\text{SM}} = \sum_{a=1}^N \frac{g_a e}{(2\pi)^2 \hbar^3 v_x v_y} \int \varepsilon_{\perp,a} \mathcal{T}(\varepsilon_{\perp,a}) f(\varepsilon_{\mathbf{k},a}) d\varepsilon_{\perp,a} d\varepsilon_{\mathbf{k},a}, \quad (\text{A2})$$

where the $\phi_{\mathbf{k}_\parallel,a}$ integration can be done by applying the identity $\int_0^{2\pi} (a^2 \cos^2 \phi_{\mathbf{k}_\parallel} + \sin^2 \phi_{\mathbf{k}_\parallel})^{-1} d\phi_{\mathbf{k}_\parallel} = 2\pi/a$ and $\partial \varepsilon_{\mathbf{k}} / \partial \varepsilon_\parallel = \varepsilon_\parallel / \varepsilon_{\mathbf{k}}$, with $\tilde{v} \equiv v_{Fy} \sqrt{(v_{Fx}/v_{Fy})^2 \cos^2 \phi_{\mathbf{k}_\parallel} + \sin^2 \phi_{\mathbf{k}_\parallel}}$. Note that for an isotropic dispersion, i.e., $v_x = v_y = v_z$, the $\phi_{\mathbf{k}_\parallel,a}$ integration is simply 2π . The superscript SM indicates a DSM or WSM. Without loss of generality, the Dirac node label a can be dropped by focusing on a Dirac node.

The ε_\perp integration then gives

$$\int |\varepsilon_\perp| \mathcal{T}(\varepsilon_\perp) d\varepsilon_\perp = D_F \int_{-\infty}^{\varepsilon_{\mathbf{k}}} |\varepsilon_\perp| e^{(\varepsilon_\perp - \varepsilon_F)/d_F} d\varepsilon_\perp, \quad (\text{A3})$$

where the approximation ($0 \rightarrow -\infty$) can be made as the emission takes place near the Fermi level and $\varepsilon_\perp \rightarrow |\varepsilon_\perp|$ can be done as the emission energy is non-negative.

Two integration regions must be considered for the upper ($\varepsilon_{\mathbf{k}} \geq 0$) and lower ($\varepsilon_{\mathbf{k}} \leq 0$) Dirac cone for the emission of electrons. Hence, Eq. (A3) becomes

$$\left(\int_0^{\varepsilon_{\mathbf{k}} \geq 0} + \int_{-\infty}^{\varepsilon_{\mathbf{k}} \leq 0} \right) |\varepsilon_\perp| e^{(\varepsilon_\perp - \varepsilon_F)/d_F} d\varepsilon_\perp. \quad (\text{A4})$$

For the upper cone,

$$\begin{aligned} & \int_0^{\varepsilon_{\mathbf{k}} \geq 0} |\varepsilon_\perp| \exp \left\{ \frac{\varepsilon_\perp - \varepsilon_F}{d_F} \right\} d\varepsilon_\perp \\ &= d_F^2 \left(\exp \left\{ \frac{\varepsilon_{\mathbf{k}} - \varepsilon_F}{d_F} \right\} \left(\frac{\varepsilon_{\mathbf{k}}}{d_F} - 1 \right) + \exp \left\{ -\frac{\varepsilon_F}{d_F} \right\} \right). \end{aligned} \quad (\text{A5})$$

For lower cone,

$$\begin{aligned} & \int_{-\infty}^{\varepsilon_{\mathbf{k}} \leq 0} |\varepsilon_\perp| \exp \left\{ \frac{\varepsilon_\perp - \varepsilon_F}{d_F} \right\} d\varepsilon_\perp \\ &= d_F^2 \exp \left\{ \frac{\varepsilon_{\mathbf{k}} - \varepsilon_F}{d_F} \right\} \left(1 - \frac{\varepsilon_{\mathbf{k}}}{d_F} \right). \end{aligned} \quad (\text{A6})$$

Hence, the solution to the ε_\perp integration can be expressed by a dimensionless tunneling function such that

$$\begin{aligned} \lambda(\varepsilon_{\mathbf{k}}/d_F) &= \text{sgn}(\varepsilon_{\mathbf{k}}) \exp \left\{ \frac{\varepsilon_{\mathbf{k}} - \varepsilon_F}{d_F} \right\} \left(\frac{\varepsilon_{\mathbf{k}}}{d_F} - 1 \right) \\ &+ \exp \left\{ -\frac{\varepsilon_F}{d_F} \right\} \left(\frac{1 + \text{sgn}(\varepsilon_{\mathbf{k}})}{2} \right), \end{aligned} \quad (\text{A7})$$

TABLE II. Relevant *ab initio* parameters used for Cd₃As₂ [63] and Na₃Bi [64].

Materials	A (eV Å)	M ₀ (eV)	M ₁ (eV Å ²)	M ₂ (eV Å ²)
Cd ₃ As ₂	2.75	-0.01	-960	-18
Na ₃ Bi	2.46	-0.0869	-10.64	-10.36

where

$$\lambda(\varepsilon_{\mathbf{k}}/d_F) = \begin{cases} \exp\left\{\frac{\varepsilon_{\mathbf{k}} - \varepsilon_F}{d_F}\right\} \left(\frac{\varepsilon_{\mathbf{k}}}{d_F} - 1\right) + \exp\left\{-\frac{\varepsilon_F}{d_F}\right\}, & \varepsilon_{\mathbf{k}} \geq 0, \\ \exp\left\{\frac{\varepsilon_{\mathbf{k}} - \varepsilon_F}{d_F}\right\} \left(1 - \frac{\varepsilon_{\mathbf{k}}}{d_F}\right), & \varepsilon_{\mathbf{k}} \leq 0. \end{cases}$$

Hence, the ε_{\perp} integration becomes

$$\int |\varepsilon_{\perp}| \mathcal{T}(\varepsilon_{\perp}) d\varepsilon_{\perp} = D_F d_F^2 \lambda(\varepsilon_{\mathbf{k}}/d_F). \quad (\text{A8})$$

This changes Eq. (14) into Eq. (15):

$$\mathcal{J}_{\perp}^{\text{SM}} = \sum_{a=1}^N \frac{c_{\text{SM},a} F^2}{\Phi t^2} D_F \int_{-\infty}^{\infty} f(\varepsilon_{\mathbf{k},a}) \lambda(\varepsilon_{\mathbf{k},a}/d_F) d\varepsilon_{\mathbf{k},a}, \quad (\text{A9})$$

where the SM represents the emission current density of a topological semimetal $c_{\text{SM}} = e^3 g / 32 m \pi^2 \hbar v_{F_x} v_{F_y}$ is a constant, with m_e being the rest mass of the electron.

The total energy distribution (TED) takes a general form of

$$P(\varepsilon_{\mathbf{k}}) d\varepsilon_{\mathbf{k}} = \frac{ge}{(2\pi\hbar)^3} \left(\int f(\varepsilon_{\mathbf{k}}) \mathcal{T}(\varepsilon_{\perp}) \frac{\Lambda_{\perp}}{\Lambda_{\parallel}} d\varepsilon_{\perp} d\phi_{\mathbf{k}_{\parallel}} \right) d\varepsilon_{\mathbf{k}}, \quad (\text{A10})$$

where the transverse density of states is defined as

$$D(\varepsilon_{\mathbf{k}}) = \int \frac{g\varepsilon_{\mathbf{k}}}{(2\pi)^2 \Lambda_{\parallel}} d\phi_{\mathbf{k}_{\parallel}} d\varepsilon_{\mathbf{k}}. \quad (\text{A11})$$

The transverse density of states vanishes at $\varepsilon_{\mathbf{k}} = 0$ and the linear $\varepsilon_{\mathbf{k}}$ term is canceled with the $1/\varepsilon_{\mathbf{k}}$ term in Λ_{\perp} . Since the TED is related to the current density by $P(\varepsilon_{\mathbf{k}}) = \partial \mathcal{J}_{\perp} / \partial \varepsilon_{\mathbf{k}}$, the TED of DSM/WSM(s) takes the form

$$P^{\text{SM}}(\varepsilon_{\mathbf{k}}) = \sum_{a=1}^N \frac{c_{\text{SM},a} D_F F^2}{\Phi t^2} f(\varepsilon_{\mathbf{k},a}) \lambda(\varepsilon_{\mathbf{k},a}/d_F). \quad (\text{A12})$$

$$\varepsilon_{\mathbf{k}} = \pm \sqrt{M_0^2 - 2M_0 M_1 k_{\perp}^2 + M_1^2 k_{\perp}^4 + (A^2 - 2M_0 M_2) k_{\parallel}^2 + M_2^2 k_{\parallel}^4 + 2M_1 M_2 k_{\perp}^2 k_{\parallel}^2}, \quad (\text{B3})$$

and hence, does not have an analytical TED solution as seen in Eq. (23). To overcome this, further simplifications can be done to the energy dispersion. First, the zero-energy solution at $(0, 0, \pm\sqrt{M_0/M_1})$ indicates the existence of two gapless bulk states along k_z at $k_{\parallel} = 0$. Next, along k_{\parallel} , the dispersion is parabolic except when $k_{\perp} = \pm\sqrt{M_0/M_1}$. Lastly, using Table II, the dominating term for Cd₃As₂ and Na₃Bi is $M_1^2 k_{\perp}^4 - 2M_0 M_1 k_{\perp}^2$ along k_z , and $(A - 2M_0 M_2) k_{\parallel}^2$ along k_{\parallel} . Hence, a minimal effective energy dispersion that can extract the characteristic from Eq. (B3) is

$$\begin{aligned} \varepsilon_{\mathbf{k}} &= \pm \sqrt{(M_0 - M_1 k_{\perp}^2)^2 + (A^2 - 2M_0 M_2) k_{\parallel}^2} \\ &= \sqrt{\varepsilon_{\perp}^2 + \varepsilon_{\parallel}^2}, \end{aligned} \quad (\text{B4})$$

APPENDIX B: DERIVATION OF TED AND \mathcal{J} USING REALISTIC HAMILTONIAN

To show that the dual-peak feature is not just an artifact from the Dirac cone approximation, the derived model can be further applied on realistic low-energy Hamiltonian for both Dirac and Weyl semimetals.

Consider the effective low-energy Hamiltonian for Cd₃As₂ and Na₃Bi [63,64] is given by

$$H_{\text{eff}} = \varepsilon_0(\mathbf{k}) + \begin{pmatrix} M(\mathbf{k}) & Ak_+ & Dk_- & B^*(\mathbf{k}) \\ Ak_- & -M(\mathbf{k}) & B^*(\mathbf{k}) & 0 \\ Dk_+ & B(\mathbf{k}) & M(\mathbf{k}) & -Ak_- \\ B(\mathbf{k}) & 0 & -Ak_+ & -M(\mathbf{k}) \end{pmatrix}, \quad (\text{B1})$$

where the four-band model in the minimal Hamiltonian is around the Γ point. Equation (B1) can be approximated to two, two-band models by expanding up to the quadratic terms, i.e., $B, D \approx 0$. Furthermore, note that $\varepsilon_0(\mathbf{k})$ is approximately an energy shift and can be set at zero. Hence, the effective energy dispersion is given by

$$\varepsilon_{\mathbf{k}} = \pm \sqrt{M^2(\mathbf{k}) + A^2 k_{\parallel}^2}, \quad (\text{B2})$$

where $M(\mathbf{k}) = M_0 - M_1 k_{\perp}^2 - M_2 k_{\parallel}^2$ and the emission direction is chosen as the z direction for consistency. The expansion of the energy dispersion involves $k_{\perp}^2 k_{\parallel}^2$ terms, i.e.,

where $\varepsilon_{\perp} = |M_0 - M_1 k_{\perp}^2|$ and $\varepsilon_{\parallel} = \sqrt{A^2 - 2M_0 M_2} k_{\parallel}$. The corresponding energy dispersion factors are

$$(\Lambda_{\perp}, \Lambda_{\parallel}) = \left(\frac{\varepsilon_{\perp}}{\varepsilon_{\mathbf{k}}}, 2(A^2 - 2M_0 M_2) \right). \quad (\text{B5})$$

Using Eq. (5), the emission current density is

$$\begin{aligned} \mathcal{J}_{\perp} &= \frac{geD_F}{(2\pi)^2 \hbar (A^2 - 2M_0 M_2)} \\ &\times \int f(\varepsilon_{\mathbf{k}}) \varepsilon_{\perp} \exp\left(\frac{\varepsilon_{\perp} - \varepsilon_F}{d_F}\right) d\varepsilon_{\perp} d\varepsilon_{\mathbf{k}}, \end{aligned} \quad (\text{B6})$$

where $\partial\varepsilon_{\mathbf{k}}/\partial\varepsilon_{\parallel} = 1/(2\varepsilon_{\mathbf{k}})$ with the transverse density of states being

$$D(\varepsilon_{\mathbf{k}}) = \frac{g\varepsilon_{\mathbf{k}}}{(2\pi)^2(A^2 - 2M_0M_2)}.$$

The replacement $\varepsilon_{\perp} \rightarrow |\varepsilon_{\perp}|$ can be made due to the absolute sign in the emission energy. The analytical \mathcal{J}_{\perp} and TED are

$$\mathcal{J}_{\perp} = \frac{geD_F d_F^2}{(2\pi)^2 \hbar(A^2 - 2M_0M_2)} \int f(\varepsilon_{\mathbf{k}}) \lambda(\varepsilon_{\mathbf{k}}/d_F) d\varepsilon_{\mathbf{k}}, \quad (\text{B7})$$

$$P(\varepsilon_{\mathbf{k}}) = \frac{geD_F d_F^2}{(2\pi)^2 \hbar(A^2 - 2M_0M_2)} f(\varepsilon_{\mathbf{k}}) \lambda(\varepsilon_{\mathbf{k}}/d_F). \quad (\text{B8})$$

Since the TED and \mathcal{J}_{\perp} are proportional to Eqs. (15) and (23), the dual-peak feature and F^3 scaling law can also be observed beyond the Dirac cone approximation for Dirac semimetals.

Similarly, this can be applied to Weyl semimetals like TaAs and TaP, with a two node minimal model with a two-band energy dispersion [65] $\varepsilon_{\mathbf{k},\pm} = \pm\sqrt{(M(k_c^2 - \mathbf{k}^2)^2 + A^2 k_{\parallel}^2)}$ with $k_c = (0, 0, \sqrt{M_0/M_1})$, which is a similar form with Eq. (B3).

-
- [1] Y.-W. Son, M. L. Cohen, and S. G. Louie, Energy Gaps in Graphene Nanoribbons, *Phys. Rev. Lett.* **97**, 216803 (2006).
- [2] T. Oka and H. Aoki, Photovoltaic Hall effect in graphene, *Phys. Rev. B* **79**, 081406(R) (2009).
- [3] G. Xu, H. Weng, Z. Wang, X. Dai and Z. Fang, Chern Semimetal and the Quantized Anomalous Hall Effect in HgCr₂Se₄, *Phys. Rev. Lett.* **107**, 186806 (2011).
- [4] B. Q. Lv, N. Xu, H. M. Weng, J. Z. Ma, P. Richard, X. C. Huang, L. X. Zhao, G. F. Chen, C. E. Matt, F. Bisti, V. N. Strocov, J. Mesot, Z. Fang, X. Dai, T. Qian, M. Shi, and H. Ding, Observation of Weyl nodes in TaAs, *Nat. Phys.* **11**, 724 (2015).
- [5] T. M. McCormick, I. Kimchi, and N. Trivedi, Minimal models for topological Weyl semimetals, *Phys. Rev. B* **95**, 075133 (2017).
- [6] Z. K. Liu, J. Jiang, B. Zhou, Z. J. Wang, Y. Zhang, H. M. Weng, D. Prabhakaran, S. K. Mo, H. Peng, P. Dudin, T. Kim, M. Hoesch, Z. Fang, X. Dai, Z. X. Shen, D. L. Feng, Z. Hussain, and Y. L. Chen, A stable three-dimensional topological Dirac semimetal Cd₃As₂, *Nat. Mater.* **13**, 677 (2014).
- [7] Z. K. Liu, B. Zhou, Y. Zhang, Z. J. Wang, H. M. Weng, D. Prabhakaran, S. K. Mo, Z. X. Shen, Z. Fang, X. Dai, Z. Hussain, and Y. L. Chen, Discovery of a three-dimensional topological Dirac semimetal, Na₃Bi, *Science* **343**, 864 (2014).
- [8] I. Crassee, R. Sankar, W. -L. Lee, A. Akrap, and M. Orlita, 3D Dirac semimetal Cd₃As₂: A review of material properties, *Phys. Rev. Mater.* **2**, 120302 (2018).
- [9] T. O. Wehling, A. M. Black-Schaffer, and A. V. Balatsky, Dirac materials, *Adv. Phys.* **63**, 1 (2014).
- [10] S.-Y. Xu, I. Belopolski, N. Alidoust, M. Neupane, G. Bian, C. Zhang, R. Sankar, G. Chang, Z. Yuan, C.-C. Lee, S.-M. Huang, H. Zheng, J. Ma, D. S. Sanchez, B. Wang, A. Bansil, F. Chou, P. P. Shibayev, H. Lin, S. Jia, and M. Z. Hasan, Discovery of a Weyl fermion semimetal and topological Fermi arcs, *Science* **349**, 613 (2015).
- [11] E. McCann and M. Koshino, The electronic properties of bilayer graphene, *Rep. Prog. Phys.* **76**, 056503 (2013).
- [12] X. Wan, A. M. Turner, A. Vishwanath, and S. Y. Savrasov, Topological semimetal and Fermi-arc surface states in the electronic structure of pyrochlore iridates, *Phys. Rev. B* **83**, 205101 (2011).
- [13] J. Xiong, S. Kushwaha, J. Krizan, T. Liang, R. J. Cava, and N. P. Ong, Anomalous conductivity tensor in the Dirac semimetal Na₃Bi, *Europhys. Lett.* **114**, 27002 (2016).
- [14] S. Wang, B.-C. Lin, A.-Q. Wang, D.-P. Yu, and Z.-M. Liao, Quantum transport in Dirac and Weyl semimetals: A review, *Adv. Phys. X* **2**, 518 (2017).
- [15] M. Lasia and L. Brey, Optical properties of magnetically doped ultrathin topological insulator slabs, *Phys. Rev. B* **90**, 075417 (2014).
- [16] B. Xu, Y. M. Dai, L. X. Zhao, K. Wang, R. Yang, W. Zhang, J. Y. Liu, H. Xiao, G. F. Chen, A. J. Taylor, D. A. Yarotski, R. P. Prasankumar, and X. G. Qiu, Optical spectroscopy of the Weyl semimetal TaAs, *Phys. Rev. B* **93**, 121110(R) (2016).
- [17] S. Polatkan, M. O. Goerbig, J. Wyzula, R. Kemmler, L. Z. Maulana, B. A. Piot, I. Crassee, A. Akrap, C. Shekhar, C. Felser, M. Dressel, A. V. Pronin, and M. Orlita, Magneto-Optics of a Weyl Semimetal beyond the Conical Band Approximation: Case Study of TaP, *Phys. Rev. Lett.* **124**, 176402 (2020).
- [18] Y. H. Choi, N. H. Jo, K. J. Lee, J. B. Yoon, C. Y. You, and M. H. Jung, Transport and magnetic properties of Cr-, Fe-, Cu-doped topological insulators, *J. Appl. Phys.* **109**, 07E312 (2011).
- [19] P.-B. Li, Z.-L. Xiang, P. Rabl, and F. Nori, Hybrid Quantum Device with Nitrogen-Vacancy Centers in Diamond Coupled to Carbon Nanotubes, *Phys. Rev. Lett.* **117**, 015502 (2016).
- [20] C. Zhu, F. Wang, Y. Meng, X. Yuan, F. Xiu, H. Luo, Y. Wang, J. Li, X. Lv, L. He, Y. Xu, J. Liu, C. Zhang, Y. Shi, R. Zhang, and S. Zhu, A robust and tuneable mid-infrared optical switch enabled by bulk Dirac fermions, *Nat. Commun.* **8**, 14111 (2017).
- [21] Q. Wang, C.-Z. Li, S. Ge, J.-G. Li, W. Lu, J. Lai, X. Liu, J. Ma, D.-P. Yu, Z.-M. Liao, and D. Sun, Ultrafast Broadband Photodetectors based on three-dimensional dirac semimetal Cd₃As₂, *Nano Lett.* **17**, 834 (2017).
- [22] L. Šmejkal, Y. Mokrousov, B. Yan, and A. H. MacDonald, Topological antiferromagnetic spintronics, *Nat. Phys.* **14**, 242 (2018).
- [23] A. B. Khanikaev, S. Hossein Mousavi, W.-K. Tse, M. Kargarian, A. H. MacDonald, and G. Shvets, Photonic topological insulators, *Nat. Mater.* **12**, 233 (2013).
- [24] Y.-Z. Yu, C.-Y. Kou, R.-L. Chern, and C.-T. Chan, Photonic topological semimetals in bianisotropic metamaterials, *Sci. Rep.* **9**, 18312 (2019).
- [25] J. Lim, Y. S. Ang, F. J. García de Abajo, I. Kaminer, L. K. Ang, and L. J. Wong, Efficient generation of extreme terahertz harmonics in three-dimensional Dirac semimetals, *Phys. Rev. Res.* **2**, 043252 (2020).
- [26] T. Zhang, K. J. A. Ooi, W. Chen, L. K. Ang, and Y. Sin Ang, Optical Kerr effect and third harmonic generation in topological Dirac/Weyl semimetal, *Opt. Express* **27**, 38270 (2019).
- [27] J. Lim, K. J. A. Ooi, C. Zhang, L. K. Ang, and Y. S. Ang, Broadband strong optical dichroism in topological Dirac semimetals with Fermi velocity anisotropy, *Chin. Phys. B* **29**, 077802 (2020).

- [28] A.-Q. Wang, X.-G. Ye, D.-P. Yu, and Z.-M. Liao, Topological semimetal nanostructures: From properties to topotronics, *ACS Nano* **14**, 3755 (2020).
- [29] S. Hofmann, C. Ducati, B. Kleinsorge, and J. Robertson, Direct growth of aligned carbon nanotube field emitter arrays onto plastic substrates, *Appl. Phys. Lett.* **83**, 4661 (2003).
- [30] S.-D. Liang and L. Chen, Generalized Fowler-Nordheim Theory of Field Emission of Carbon Nanotubes, *Phys. Rev. Lett.* **101**, 027602 (2008).
- [31] S. Zhou, K. Chen, M. T. Cole, Z. Li, J. Chen, C. Li, and Q. Dai, Ultrafast field-emission electron sources based on nanomaterials, *Adv. Mater.* **31**, 1805845 (2019).
- [32] F. Giubileo, A. Di. Bartolomeo, L. Iemmo, G. Luongo, and F. Urban, Field emission from carbon nanostructures, *Appl. Sci.* **8**, 526 (2018).
- [33] L. Chen, H. Yu, J. Zhong, L. Song, J. Wu, and W. Su, Graphene field emitters: A review of fabrication, characterization and properties, *Mater. Sci. Eng. B* **220**, 44 (2017).
- [34] S. Sun, L. K. Ang, D. Shiffler, and J. W. Luginsland, Klein tunnelling model of low energy electron field emission from single-layer graphene sheet, *Appl. Phys. Lett.* **99**, 013112 (2011).
- [35] Y. Ang, S.-J. Liang, and L. Ang, Theoretical modeling of electron emission from graphene, *MRS Bull.* **42**, 505 (2017).
- [36] X. Wei, Y. Bando, and D. Golberg, Electron emission from individual graphene nanoribbons driven by internal electric field, *ACS Nano* **6**, 705 (2012).
- [37] S.-J. Liang and L. K. Ang, Electron Thermionic Emission from Graphene and a Thermionic Energy Converter, *Phys. Rev. Appl.* **3**, 014002 (2015).
- [38] Y. S. Ang, H. Y. Yang, and L. K. Ang, Universal Scaling Laws in Schottky Heterostructures Based on Two-Dimensional Materials, *Phys. Rev. Lett.* **121**, 056802 (2018).
- [39] Y. S. Ang, Y. Chen, C. Tan, and L. K. Ang, Generalized High-Energy thermionic Electron Injection at Graphene Interface, *Phys. Rev. Appl.* **12**, 014057 (2019).
- [40] S. Huang, M. Sanderson, Y. Zhang, and C. Zhang, High efficiency and non-Richardson thermionics in three dimensional Dirac materials, *Appl. Phys. Lett.* **111**, 183902 (2017).
- [41] Y. S. Ang, L. Cao, and L. K. Ang, Physics of electron emission and injection in two-dimensional materials: Theory and simulation, *InfoMat* **3**, 502 (2021).
- [42] R. G. Forbes, Simple good approximations for the special elliptic functions in standard Fowler-Nordheim tunneling theory for a Schottky-Nordheim barrier, *Appl. Phys. Lett.* **89**, 113122 (2006).
- [43] R. G. Forbes and J. H. Deane, Reformulation of the standard theory of Fowler-Nordheim tunnelling and cold field electron emission, *Proc. R. Soc. London Ser. A* **463**, 2907 (2007).
- [44] K. L. Jensen and M. Cahay, General thermal-field emission equation, *Appl. Phys. Lett.* **88**, 154105 (2006).
- [45] L. W. Swanson, L. C. Crouser, and F. M. Charbonnier, Energy exchanges attending field electron emission, *Phys. Rev.* **151**, 327 (1966).
- [46] M. Dionne, S. Coulombe, and J.-L. Meunier, Energy exchange during electron emission from carbon nanotubes: Considerations on tip cooling effect and destruction of the emitter, *Phys. Rev. B* **80**, 085429 (2009).
- [47] M. S. Chung, Energy exchange processes in electron emission at high fields and temperatures, *J. Vac. Sci. Technol. B* **12**, 727 (1994).
- [48] V. T. Binh, N. Garcia, and S. Purcell, Electron Field Emission from Atom-Sources: Fabrication, Properties, and Applications of Nanotips, in *Advances in Imaging Electron Physics* (Elsevier, Amsterdam, 1996), Vol. 95, pp. 63–153.
- [49] R. D. Young, Theoretical total-energy distribution of field-emitted electrons, *Phys. Rev.* **113**, 110 (1959).
- [50] J. W. Gadzuk and E. W. Plummer, Field emission energy distribution (FEED), *Rev. Mod. Phys.* **45**, 487 (1973).
- [51] J. Lee, Y. Jung, J. Song, J. S. Kim, G.-W. Lee, H. J. Jeong, and Y. Jeong, High-performance field emission from a carbon nanotube carpet, *Carbon N.Y.* **50**, 3889 (2012).
- [52] N. de Jonge, M. Allieux, J. T. Oostveen, K. B. K. Teo, and W. I. Milne, Optical Performance of Carbon-Nanotube Electron Sources, *Phys. Rev. Lett.* **94**, 186807 (2005).
- [53] L. Li, W. Sun, S. Tian, X. Xia, J. Li, and C. Gu, Floral-clustered few-layer graphene nanosheet array as high performance field emitter, *Nanoscale* **4**, 6383 (2012).
- [54] E. L. Murphy and R. H. Good, Thermionic emission, field emission, and the transition region, *Phys. Rev.* **102**, 1464 (1956).
- [55] G. S. Jenkins, C. Lane, B. Barbiellini, A. B. Sushkov, R. L. Carey, F. Liu, J. W. Krizan, S. K. Kushwaha, Q. Gibson, T.-r. Chang, H.-t. Jeng, H. Lin, R. J. Cava, A. Bansil, and H. D. Drew, Three-dimensional Dirac cone carrier dynamics in Na₃Bi and Cd₃As₂, *Phys. Rev. B* **94**, 085121 (2016).
- [56] Z. Huang, Y. Jiang, Q. Han, M. Yang, J. Han, F. Wang, M. Luo, Q. Li, H. Zhu, X. Liu, J. Gou, and J. Wang, High responsivity and fast UV-vis-short-wavelength IR photodetector based on Cd₃As₂/MoS₂ heterojunction, *Nanotechnology* **31**, 064001 (2020).
- [57] C.-C. Lee, S.-Y. Xu, S.-M. Huang, D. S. Sanchez, I. Belopolski, G. Chang, G. Bian, N. Alidoust, H. Zheng, M. Neupane, B. Wang, A. Bansil, M. Z. Hasan, and H. Lin, Fermi surface interconnectivity and topology in Weyl fermion semimetals TaAs, TaP, NbAs, and NbP, *Phys. Rev. B* **92**, 235104 (2015).
- [58] S. Chi, Z. Li, Y. Xie, Y. Zhao, Z. Wang, L. Li, H. Yu, G. Wang, H. Weng, H. Zhang, and J. Wang, Ultra-broadband photodetection of Weyl semimetal TaAs up to infrared 10 μm range at room temperature, [arXiv:1705.05086](https://arxiv.org/abs/1705.05086).
- [59] D. Grassano, O. Pulci, A. Mosca Conte, and F. Bechstedt, Validity of Weyl fermion picture for transition metals monpnictides TaAs, TaP, NbAs, and NbP from *ab initio* studies, *Sci. Rep.* **8**, 3534 (2018).
- [60] Z. Du, F. Jiang, J. Zheng, S. Chen, F. Gao, J. Teng, D. Fu, H. Zhang, and W. Yang, Field emission behaviors of CsPbI₃ nanobelts, *J. Mater. Chem. C* **8**, 5156 (2020).
- [61] T. Berry, L. A. Pressley, W. A. Phelan, T. T. Tran, and T. M. McQueen, Laser-enhanced single crystal growth of non-symorphic materials: Applications to an eight-fold fermion candidate, *Chem. Mater.* **32**, 5827 (2020).
- [62] R. G. Forbes, Refining the application of Fowler-Nordheim theory, *Ultramicroscopy* **79**, 11 (1999).
- [63] S. Jeon, B. B. Zhou, A. Gyenis, B. E. Feldman, I. Kimchi, A. C. Potter, Q. D. Gibson, R. J. Cava, A. Vishwanath, and A. Yazdani, Landau quantization and quasiparticle interference in the three-dimensional Dirac semimetal Cd₃As₂, *Nat. Mater.* **13**, 851 (2014).

- [64] Z. Wang, Y. Sun, X. Q. Chen, C. Franchini, G. Xu, H. Weng, X. Dai, and Z. Fang, Dirac semimetal and topological phase transitions in A_3Bi ($A = Na, K, Rb$), *Phys. Rev. B* **85**, 195320 (2012).
- [65] S.-Q. Shen, *Topological Insulators: Dirac Equation in Condensed Matter*, Springer Series in Solid-State Sciences, Vol. 187 (Springer, Singapore, 2017), p. 266.
- [66] A. A. Abrikosov, Gapless state of bismuth-type semimetals, *J. Low Temp. Phys.* **8**, 315 (1972).
- [67] A. Akrap, M. Hakl, S. Tchoumakov, I. Crassee, J. Kuba, M. O. Goerbig, C. C. Homes, O. Caha, J. Novák, F. Teppe, W. Desrat, S. Koohpayeh, L. Wu, N. P. Armitage, A. Nateprov, E. Arushanov, Q. D. Gibson, R. J. Cava, D. van der Marel, B. A. Piot *et al.*, Magneto-Optical Signature of Massless Kane Electrons in Cd_3As_2 , *Phys. Rev. Lett.* **117**, 136401 (2016).
- [68] Y. Baba, Á. Díaz-Fernández, E. Díaz, F. Domínguez-Adame, and R. A. Molina, Electric field manipulation of surface states in topological semimetals, *Phys. Rev. B* **100**, 165105 (2019).
- [69] H. Pan, M. Wu, Y. Liu, and S. A. Yang, Electric control of topological phase transitions in Dirac semimetal thin films, *Sci. Rep.* **5**, 14639 (2015).
- [70] N. P. Armitage, E. J. Mele, and A. Vishwanath, Weyl and Dirac semimetals in three-dimensional solids, *Rev. Mod. Phys.* **90**, 015001 (2018).
- [71] V. Litovchenko, A. Evtukh, M. Semenenko, A. Grygoriev, O. Yilmazoglu, H. L. Hartnagel, L. Sirbu, I. M. Tiginyanu, and V. V. Ursaki, Electron field emission from narrow band gap semiconductors (InAs), *Semicond. Sci. Technol.* **22**, 1092 (2007).
- [72] K. A. Abdul Khalid, T. J. Leong, and K. Mohamed, Review on thermionic energy converters, *IEEE Trans. Electron Devices* **63**, 2231 (2016).
- [73] P. Zhang, Y. S. Ang, A. L. Garner, Á. Valfells, J. W. Luginsland, and L. K. Ang, Space-charge limited current in nanodiodes: Ballistic, collisional, and dynamical effects, *J. Appl. Phys.* **129**, 100902 (2021).